Int J Earth Sci (Geol Rundsch) (2006) 95: 189–203
DOI 10.1007/s00531-005-0034-x

ORIGINAL PAPER

M. Seyferth · A. Henk

A numerical sandbox: high-resolution distinct element models of halfgraben formation

Received: 3 May 2004 / Accepted: 23 November 2004 / Published online: 14 December 2005

Abstract Basin-scale tectonics and sedimentation are studied using particle flow code (PFC), a special implementation of the distinct-element method (DEM) using circular elements. Special focus is on the development and application of new techniques, which allow for strain weakening and localisation effects and, thus, the formation of discrete fault patterns in high-resolution DE models.Fundamental modelling assumptions and the procedures necessary to define the microproperties of a DE material from given rock mechanical data are first explained. Recent methodical enhancements, consisting of automatic fault detection (AFD) and intelligent crack management (ICM) algorithms are also discussed. Refined DE modelling techniques are then applied to three scenarios of extensional basin formation, i.e. the evolution of halfgrabens above detachments with simple listric and ramp–flat–ramp geometries, respectively. Numerical modelling results compare favourably with the analogue ('sandbox') models widely used in this kind of basin studies. Not only do they reproduce the general basin architecture (e.g. roll-over anticlines and crestal collapse grabens), but also detailed fault structure and the sequence of faulting. In addition, numerical models can describe temporal changes in mechanical material properties to model compaction and diagenesis of syntectonic sediments.

Keywords Distinct element method · Finite element method · Numerical modeling · Halfgraben

Introduction

The distinct-element method (DEM), a group of numerical discontinuum modelling approaches, offers a number of advantages over continuum methods. In particular, it allows fracturing and unlimited differential displacements between individual elements. PFC2D (Particle Flow Code in 2 Dimensions; Itasca Consulting Group, Minneapolis, USA), a special DEM code, is based on circular elements and the fundamental laws of contact physics (Cundall 1971; Cundall and Strack 1979; Itasca 1999). Thus, it is ideal to simulate the rheological behaviour of granular materials. PFC2D elements can also be bonded to describe consolidated rock and, in turn, bond breakage can be used to study fracture mechanics. The code has been successfully applied to various industrial and geotechnical problems such as mining (e.g. Sainsbury et al. 2003; Diederichs et al. 2004), rock mechanics (e.g. Holt et al. 2003) and slope stability (e.g. Wang et al. 2003).

PFC2D and similar codes also provide interesting tools to study the fundamental problems of crustal deformation in the brittle domain. Some published work has been focused on the mechanics of individual faults or shear-zones, providing detailed information on the processes accommodating localised shear strain, the resulting sliding friction and the formation of fault gouges (e.g. Mora and Place 1998; Morgan and Boettcher 1999). Others have addressed the spatial distribution of seismic events and the short-time response of adjacent rocks (Mora and Place 1993; Scott 1996; Dalguer et al. 2003). A third group intended to approximate the large-scale kinematics of geodynamic processes, even of those that can hardly be addressed by continuum models due to the large amounts of deformation (Erickson et al. 2001; Burbidge and Braun 2002; Strayer and Suppe 2002; Vietor 2003). In summary, published DE models are either limited in their spatial extent, the covered time interval or the model resolution (i.e. large element size). Moreover, in some studies, fracture directions might be biased by the regular packing of elements.

In this study, basin-scale models of tectonics and sedimentation, which cover geological time scales and are detailed enough to simulate displacements along

M. Seyferth · A. Henk (✉)
Geologisches Institut, Universität Freiburg,
Albertstr. 23 b, 79104 Freiburg, Germany
E-mail: henk@uni-freiburg.de
Tel.: +49-761-2036471

individual faults, are presented. To do so, new modelling techniques, which allow for strain localisation and discrete fracture formation in irregularly packed and thus isotropic PFC2D materials, have been developed. In combination with parallel processing, these techniques are fundamental for a detailed simulation of basin-scale tectonics and sedimentation. The second part of the paper shows some applications of this refined DEM and presents high-resolution models of halfgraben formation. The numerical models are compared to analogue, i.e. 'sandbox', experiments that are traditionally used in this kind of basin-scale studies, and the benefits and limitations of the DEM models are also discussed.

Background

PFC2D: general features

While the computations of PFC2D are strictly limited to two dimensions, a unit thickness is assumed in order to calculate mass; consequently, the individual elements will be referred to as 'discs' in this study. Assemblages of discs are termed 'synthetic materials' if they are designed to approximate granular or brittle behaviour of natural materials. Interactions of discs in a synthetic material and their response to applied boundary conditions, are computed by an explicit finite-difference approach (Itasca 1999) using a large number of individual calculation cycles.

During each of these cycles, the current contacts between discs are first detected and then a linear force–displacement law is applied to each of them (Figs. 1, 2a).Interpenetration between neighbouring discs is controlled by their mechanical *microproperties* and the applied forces (e.g. boundary forces, gravity). Microproperties refer to individual discs (or individual disc contacts) and are not directly related to the bulk properties (*macroproperties*) of the synthetic material. Standard microproperties comprise the normal and shear stiffness components k_n and k_s, as well as friction μ_d and density ρ_d (Fig. 1). The synthetic materials used in this study are further characterised by breakable bonds tying discs in contact, which bear normal F_c^n and shear strength F_c^s as additional microproperties. All relevant symbols used in the text are listed in Table 1.

In the second step of the calculation cycle, Newton's law of motion (Fig. 2a) is used to calculate the resultant disc acceleration. The circular shape and the simple mechanical behaviour of PFC2D discs strongly accelerate these computations and, thus, allow us to consider a large number of elements and high model resolutions, respectively. Explicit solution of the resulting differential equations precludes taking into account the real time span of long-term geodynamic problems in the model calculations. However, a quasi-static approach can be used if the inertial term in a multi-body system, governed by Coulomb friction, is negligible when compared to dissipative forces (e.g. Peshkin and Sanderson 1989).

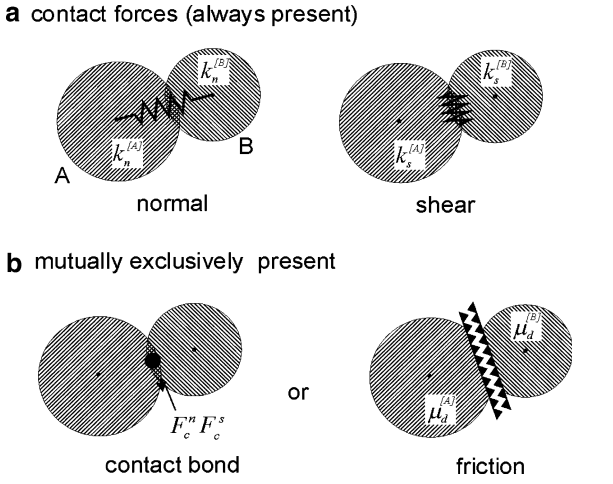

Fig. 1 Basic mechanical interactions between two discs, as implemented in PFC2D. (**a**) Based on the stiffness microproperties (k_n, k_s) of the discs, a contact law defines the respective contact forces; (**b**) if a contact-bond is present, it is governed by the bond strength components (F_c^n, F_c^s); if no bond is present or an existing bond has failed, the microproperty friction (μ_d) controls whether or not slip occurs at the contact

This applies to brittle deformation, if static friction can be assumed to be time-independent. In PFC2D the kinetic energy is either dissipated by plastic (frictional) yielding or by a mechanical damping term. The type of damping embodied in PFC2D is local and non-viscous, i.e. it acts to suppress accelerating motion rather than velocity. In this way, steady motion is not inhibited (Itasca 1999). However, it has to be assured that velocities induced by boundary conditions are slow enough to affect the whole system and to preclude boundary effects. This condition is tested by comparing the *mean unbalanced force* (acting on discs), *mean contact force* (between discs) and *maximum unbalanced force* in the system.

Modelling tectonics and sedimentation

Brittle deformation

If large portions of rocks are assumed to host statistically scattered pre-existing cracks, their first-order mechanical behaviour can be described by empiric laws predicting the depth dependence of peak strength, which controls the onset of frictional sliding along pre-existing planes (Byerlee 1978). Formally, they are identical to the Mohr–Coulomb failure criterion $\tau_{crit} = c + \mu \sigma'_n$ (where μ_{crit} is the critical shear stress, σ'_n the effective normal stress, μ the static friction coefficient and c the cohesion). The effective normal stress σ'_n may be reduced by the presence of pore fluid under isotropic pressure conditions (Hubbert and Rubey 1959). According to Byerlee's (1978) laboratory sliding experiments, τ_{crit} is rather independent of the rock type and amounts to $\tau_{crit} = 0.85\sigma'_n$; at normal stresses

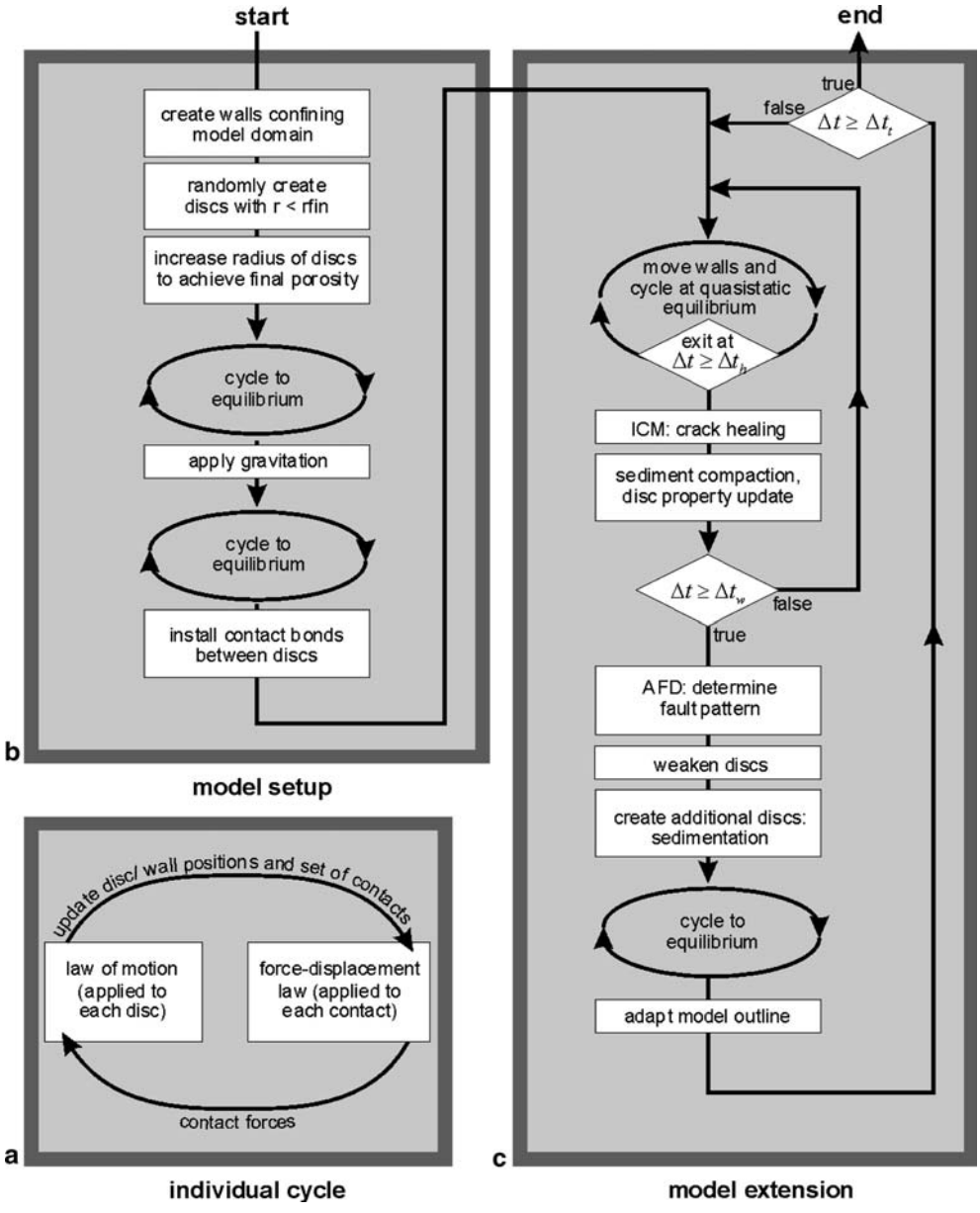

Fig. 2 **a** Individual PFC calculation cycle; during a typical model run, more than one million cycles are computed. **b** Workflow diagram illustrating the setup. **c** Subsequent extension of the numerical models. *Symbols* are explained in Table 1

$\sigma_n < 200$ MPa and $\tau_{crit} = 60$ MPa $+ 0.6\sigma'_n$ at larger normal stresses, respectively. Synthetic DE materials approximating Byerlee behaviour (e.g. MAT18-B, see calibration data below) have shown plausible large-scale deformation patterns (Seyferth and Henk 2002), but the localisation of deformation along 'discrete faults' is much less pronounced than in equivalent analogue models (e.g. Ellis and McClay 1988; McClay 1989). More precisely speaking, granular shear zones (Fig. 3), which are the model representations of discrete faults in both types of models, usually span some 10^1–10^2 disc diameters in numerical models (e.g. Mora and Place 1998; Morgan and Boettcher 1999), while their extent in sandbox-models is only about 5 grain diameters (McClay 1989). This is due to the more efficient strain memory inherent in materials composed of particles that are not perfectly rounded (e.g. natural sand). Since relative displacement along a granular shear zone has to be large when compared to the particle diameters, in order to initialise strain memory by rotating and/or sorting of the particles, lower resolving numerical models are hampered by an additional drawback. In practise, computing costs significantly rise if angular particles are employed and/or the model resolution increased, Thus, they limit the scope of most DE models to the dynamics of single faults or shear zones.

In natural rocks, different processes control the degree of strain localisation on large-scale faults as well as the importance of diffuse small-scale displacements. In general, only a small minority of potential dislocation planes is tectonically active, whereas most others accommodate only small or no relative displacements. Thereby, activity is not only controlled by the orientation of a plane, but also by its length, its intercon-

Table 1 Units, symbols and their (default) values addressing model setup, boundary conditions, microparameters, localisation algorithms and syn-rift sediments

Model geometry, discretisation and boundary conditions			
Maximum hanging wall thickness	M	1.5×10^{4}	
Hanging wall length	M	5×10^{4}	
Average disc radius $\bar{r}_d$	M	0.931×10^{2}	
Disc radius ratio r_d^{max}/r_d^{min}	–	1.66	
Porosity of disc assemblage Φ_d^a	–	0.17	
Extension rate	m a^{-1}	1×10^{-2}	
Total extension time Δt_t	a	1×10^{6}	
Microparameters of synthetic materials		MAT 18-B	MAT 18-W
Bulk density ρ_{tot} [b]	kg m^{-3}	2.6×10^{3}	2.6×10^{3}
Disc density ρ_d	kg m^{-3}	3.042×10^{3}	Depth-dependent[c]
Disc friction μ_d	–	5.0×10^{-2}	0.0
Normal disc stiffness quotient k_n	Pa	1.7×10^{11}	8.5×10^{8}
Shear disc stiffness k_s	Pa	6.38×10^{10}	3.259×10^{8}
Average tensile bond strength $\bar{F}_c^n$	N	2.0×10^{4}	0.0
Standard deviation of tensile bond strength F_c^n	N	0.5×10^{4}	0.0
Average shear bond strength $\bar{F}_c^s$	N	2.0×10^{8}	0.0
Standard deviation of shear bond strength F_c^s	N	0.5×10^{8}	0.0
Disc weakening (AFD)			
Time increment Δt_w	a	5×10^{4}	
Minimum strain-rate $\dot{\varepsilon}_{cw}$	s^{-1}	1×10^{-13}	
Minimum fault distance l_{csp}	m	5×10^{3}	$\approx 5\cdot\bar{r}_d$
Crack healing (ICM)			
Time increment Δt_h	a	2.5×10^{3}	
Maximum strain-rate $\dot{\varepsilon}_{ch}$	s^{-1}	1×10^{-15}	
Syn-rift sedimentation and diagenesis			
Time increment sedimentation Δt_s	a	5×10^{4}	$=\Delta t_w$
Surface porosity of sediments Φ_{ini}	–	0.5	
Time increment sediment compaction Δt_d	a	2.5×10^{3}	$=\Delta t_h$
Porosity-depth coefficient c	m^{-1}	0.4	

[a]Porosity of the synthetic material due to disc packing; values are slightly modified when gravity is applied
[b]Disc densities are calculated using the final porosity of the disc assemblage
[c]Due to large disc-interpenetration at high surrounding pressures, disc radii and densities are modified based on the current position of the individual disc

nectivity to other planes and the effect of different long-term mechanical or chemical fault-zone weakening processes that lead to the formation of fault gouges and other cataclastic rocks (for a summary see Rutter et al. 2001). In the model, we account for these processes by employing a significantly weakened material MAT18-W, which is used along planes of large relative displacements; some details concerning the weakening process and the calibration data are described in the section 'Enhanced DE models using AFD and ICM techniques'.

Syn-rift sedimentation and diagenetic processes

The addition (or removal) of material during a model run by exogenic processes is simulated by a universal algorithm, which can adapt the model outline to any arbitrary target geometry and, at the same time, installs gravitationally pre-stressed conditions. In detail, the procedure encompasses the creation of additional discs, their gravitational settling to equilibrium conditions and the subsequent modification of disc radii until fit with the target geometry is achieved. During a model run, sedimentation of upto 20 different strata, and their subsequent subsidence, can be recorded.

Newly formed syn-rift sediments are represented by an unbonded material, with a significantly reduced density in order to account for large surface porosities ($\Phi_{ini}=0.5$). Subsequently, mechanical material properties of the sediments change during burial and related diagenesis, i.e. compaction and cementation. In the numerical model, this is simulated by volume loss and contemporaneous density increase of individual discs. The calculation is based on the porosity at the current burial depth $\Phi(y)=\Phi_{ini}e^{-cy}$, where c is the porosity-depth coefficient (Baldwin and Butler 1985). The effects of cementation, on the other hand, are simulated by contact-bonds, which are increasingly created by the ICM algorithm (see the section 'Enhanced DE models using AFD and ICM techniques') during burial and compaction.

Enhanced modelling techniques

The materials used in this study were irregularly arranged and contact-bonded in a manner similar to that employed by Strayer and Suppe (2002). Others workers have used regular disc arrangements (e.g. Saltzer and Pollard 1992; Burbidge and Braun 2002) and granular materials only controlled by coulomb friction (e.g. Vietor 2003), respectively. Irregular disc arrangement

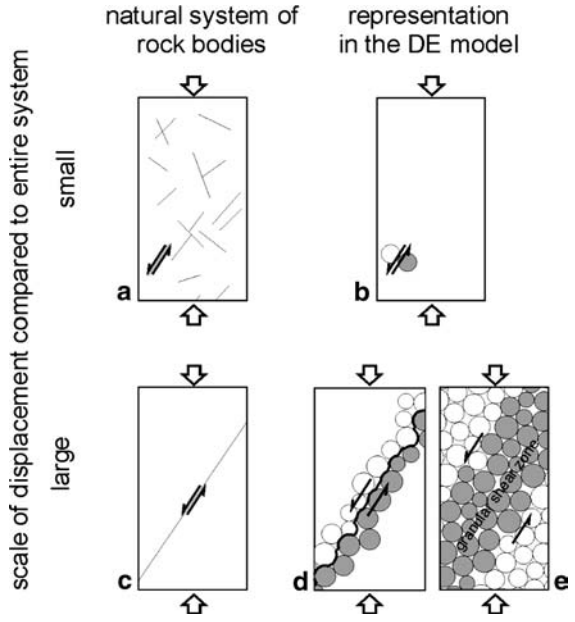

Fig. 3 Concepts of strain localisation in particle models. (**a**) Slip along an individual small-scale fault within a larger portion of rock is adequately represented by (**b**) contact-bond failure and subsequent slip between individual discs in the model. In contrast, (**c**) representation of significant displacements along larger-scale faults requires slip along the virtual boundary between two blocks, which is characterised by (**d**) significant asperities resulting from the actual disc pattern. Even if there are no contact-bonds present across this boundary and microscopic disc friction is zero, there is significant macroscopic friction since blocks get stuck at discs protrusions. Thus, slip is accommodated in a more efficient manner by (**e**) dilation processes within a broad granular shear zone

provides statistical isotropy of the material and precludes geometry-dependent preferred slip orientation (i.e. angles of 30 and 60° at hexagonal disc packing). Contact-bonds between neighbouring discs characterised by normal and shear strength (F_c^n and F_c^s) are used to intensify initial localisation of strain. While breakage of bonds occurs when yield strength is overcome, strain-dependent healing (re-installation) of bonds has been implemented by means of the ICM algorithm. Finally, the materials used in this study are controlled by depth-dependent strength and show a single-stage strain-dependent weakening behaviour.

Since the behaviour of a synthetic material cannot be defined in a direct manner and depends on a complex interplay between disc microproperties and geometric features of the disc assembly, they have to be tuned in during a multi-stage iterative calibration process. This procedure comprises: (1) the calibration of elastic material parameters, (2) the subsequent implementation of depth-dependent yield strength using a displacement-driven biaxial test; (3) the calibration of a modified (weakened) synthetic material which allows significant displacements to occur along larger-scale localised shear-zones by a modified displacement-driven shear-box test, and (4) the validation of weakening along shear zones and the healing of broken bonds controlled by critical strain-rates.

Material setup and testing

The iterative calibration procedure encompasses repeated changes in the material's microproperties, each followed by a testing of the resulting macroproperties. To investigate the elastic properties of a given synthetic material, a numerical test based on a setup provided by Itasca (1999) was used, which mimics a standard displacement-driven uniaxial laboratory test. The appropriateness of the test setup has been intensely validated by testing different initial disc configurations and variant sample sizes (Seyferth, submitted). Samples used in this study are characterised by 'natural' sample dimensions of 4,000×2,000 m (Fig. 4a), comprising about 200 discs with a mean radius of $\bar{r}_d = 93.1$ m and a radius ratio $r_d^{max}/r_d^{min} = 1.66$. This is also the disc size range used in the final halfgraben experiments.

Typical elastic properties of upper crustal rocks are a Young's modulus of 50 GPa and a Poisson's ratio of 0.25. To perform the uniaxial test, σ_3 is set to zero and a network of strong contact-bonds is installed to prevent plastic deformation. Young's modulus is adjusted by variations of the disc stiffness microproperties k_n and k_s. Then, an adequate Poisson's ratio can be tuned in by modifying the k_n/k_s ratio and the desired values are best approximated by relatively large k_n/k_s ratios.

Since crustal deformation upto a depth of 15 km should be addressed by these models, depth-dependence of the yield strength (as described by Byerlee's relationships) has to be reproduced over some orders of magnitude. Yield strength does not automatically increase with surrounding pressure in contact-bonded synthetic materials, since it is strongly dependent on the strength of the bonds. A biaxial version of the test set-up described above, is used to determine the material's yield strength under variable confining pressures (σ_3), which are applied laterally by a servo-logic (Fig. 4a, b). As proposed by Itasca (1999), the dependence of yield strength on σ_3 can be achieved by modifying the ratio between shear and normal strength F_c^s/F_c^n of the contact-bonds. The results of biaxial testing indicate that F_c^s values significantly exceeding F_c^n (i.e. by a factor of 10^4), are appropriate; under such circumstances, almost every bond failure on the microscale is triggered by extensional forces that are most likely to occur under small confining pressures. Uni- and biaxial testing results in best-fit microproperties (Table 1) that characterise the synthetic material MAT18-B ('bonded').

Weakened materials

MAT18-B is capable of producing depth-dependent yield strength, but deformation is poorly localised along broad and short-lived granular shear zones. Since broken contact-bonds are not re-installed when slip-rates decrease, significant strain-weakening affects large areas in the model. To enhance the degree of strain localisation and to recognise individual 'discrete faults' in the

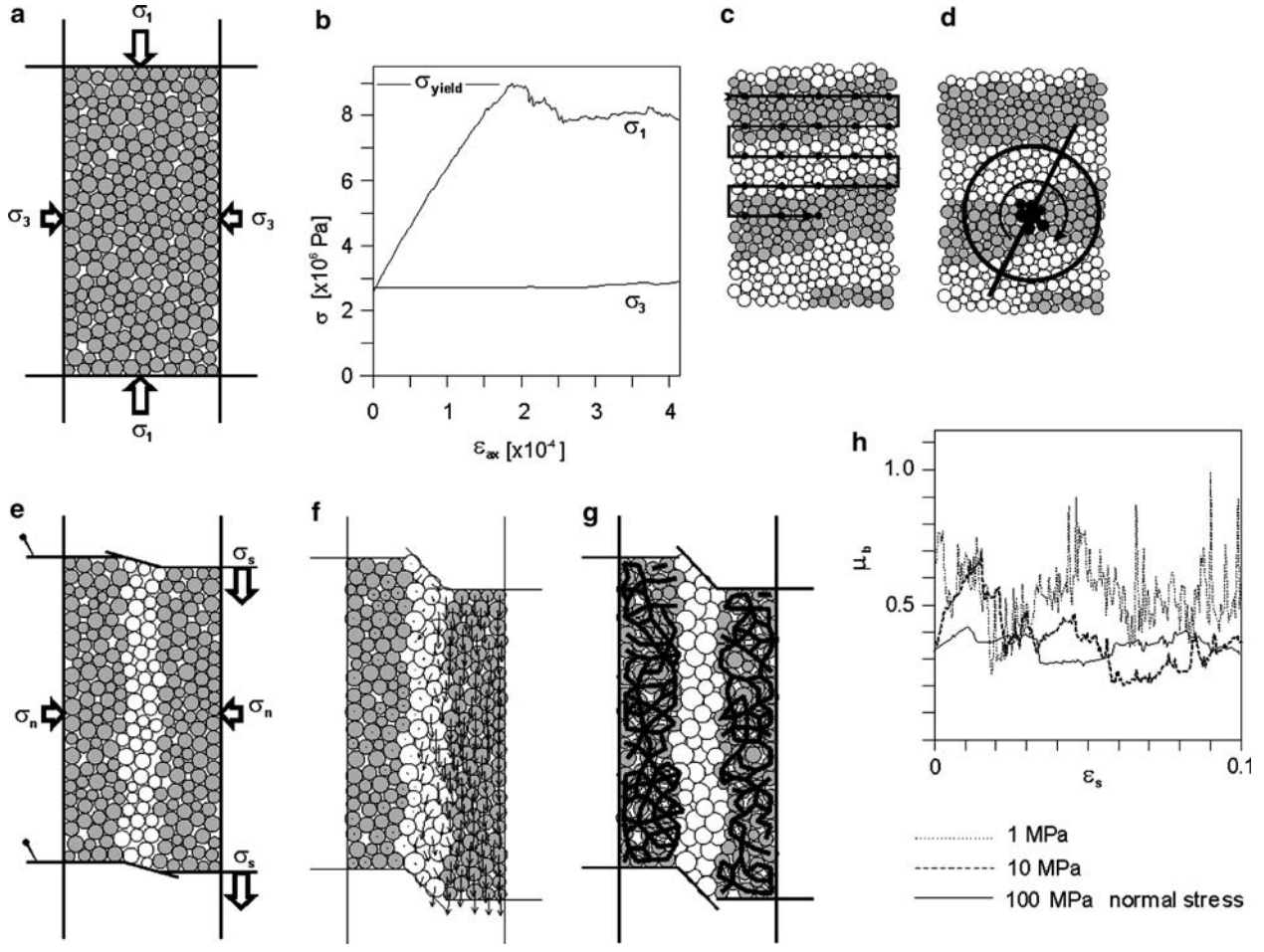

Fig. 4 Tools to evaluate and modify the mechanical behaviour of synthetic materials. (**a**) The large-scale deformation behaviour of a rock sample is tested by a uni-/biaxial testing setup that reveals (**b**) the relationships of stresses and axial strain ε_{ax}, as well as the yield strength of a sample consisting of MAT18-B. (**c**) The AFD algorithm scans the model domain and (**d**) investigates potential fault planes at different dip angels, in order to detect sites of large slip; discs in the centre of the measure circle (*black*) may be weakened if the displacement is large enough. (**e**) The mechanical behaviour of narrow shear zones can be studied by using a modified shear-box test. Tests with a sufficiently weakened material, MAT18-W, in the centre of the sample (*white discs*) show (**f**) a large displacement gradient and (**g**) contact-bonds outside the intended shear zone remain intact. (**h**) Bulk friction μ_b (vs shear strain ε_s) is around 0.5 for normal stress varying over a broad range

model, additional material testing has been performed based on the assumption that an efficient granular shear-zone should be localised to a width about three times the mean disc diameter (cf. also Itasca 1999). Thereby, a modified shear box test limits the extent of the shear along an intended shear-zone of 600 m width (Fig. 4e–g). Bulk friction μ_b is the ratio of measured shear stress over normal stress σ_s/σ_n. While σ_n is applied by a servo-logic, σ_s is measured at the box walls, which are moved at a constant and sufficiently small shear velocity. If a sample of MAT18-B is tested, the pattern of failed contact-bonds indicates that the slip is accommodated by dilation processes, which largely exceed the imposed shear-zone and, thus, MAT18-B is not capable of hosting a narrow granular shear-zone. Moreover, if MAT18-B is sandwiched between elastic blocks to simulate a shear-zone of limited extent, friction is about twice as large as that proposed by Byerlee's relationship. Consequently, in order to allow for efficient sliding that is strictly limited to the narrow shear-zone, a significantly weaker material MAT18-W has been calibrated that obeys Byerlee's behaviour in a localised manner. This material not only had to be microscopically frictionless ($\mu_d = 0$) and unbonded, but also disc stiffnesses had to be reduced by a factor of 200 (Table 1). Finally, re-implantation of MAT18-W into a vice consisting of MAT18-B, has proved that sliding friction is in the desired range (Fig. 4h) and that bond pattern remains intact outside, in MAT18-B (Fig. 4f, g).

Enhanced DE models using AFD and ICM techniques

The behaviour of a system of natural rock bodies separated by faults or shear zones can be adequately modelled using MAT18-B (to approximate elastic-diffusely plastic deformation) and MAT18-W (to simulate localised slips along pre-defined faults). In order to

simulate self-organised fault formation and growth, however, an automatic and reproducible fault-zone detection technique has been developed (Seyferth and Henk 2003; Seyferth submitted).

The automatic fault-zone detection (AFD) algorithm determines single fault segments using a criterion of minimum relative shear displacement d_{cw} (derived from a minimum shear strain-rate $\dot{\varepsilon}_{cw}$, for a time interval Δt_w, between the two halves of a measured circle, which are separated by a proposed fault. The whole model domain was scanned using this measure circle (Fig. 4c) and several fault angles were checked at any given sampling point (Fig. 4d). Fault-parallel displacement components of individual discs are integrated on either side of the proposed fault, resulting in the actual shear displacement d_w. A real clustering of detected shear zones in high-strain zones is prevented by applying a minimum fault spacing criterion that ignores proposed faults closer than five average disc diameters to a more active fault. If $d_w > d_{cw}$ and the minimum spacing criterion apply, discs in the centre of the measure circle are weakened by replacing MAT18-B by MAT18-W. This procedure allows for the continuous sliding along shear zones without explicitly weakening the modelled rocks in a geological sense. Disc weakening may rather be interpreted as a process of connecting small-scale cracks and organising systems of linked dislocation planes, which are capable to accommodate shear strain efficiently. Detailed information about the mathematical background of the procedure and its practical implementation are available at Seyferth (submitted).

The intelligent crack management (ICM) algorithm is an extension of PFD2D's contact-bond logic (Itasca 1999) by a strain-rate dependent bond re-installation (i.e. healing) criterion. The critical maximum relative displacement d_{ch} (for the time interval Δt_h), between two discs after a time interval Δt_h, is deduced from a critical maximum shear strain-rate $\dot{\varepsilon}_{ch}$. Comparing the actual relative displacements d_h, determined from the current model geometry, it is found to decide whether the rupture persists or a contact-bond is re-installed. Potential subsequent bond breakage is then controlled again by the stress-dependent criterion provided by PFC2D (Itasca 1999). Since individual contacts between two discs do not represent single natural planes, but are rather proxies describing the mechanical behaviour of a larger portion of rock (some 10^5 m^2 at current resolution) over a considerable time step, a geological interpretation of bond failure and healing may be as follows: intact bonds indicate low strain, which is accommodated predominantly in an elastic manner; temporal increase in strain with likely fault activity is expressed by bond failure; an unbonded contact indicates large strain, which may be accommodated by further fault slip; and finally, bond healing may stand for a temporal decrease in strains where the healing of fault planes is likely.

Summarising, enhanced tectonic DE models using MAT18-B and MAT18-W, linked via the AFD and ICM algorithms, account for the following four different states of rock behaviour (Fig. 5). (1) From a macroscopic point of view, unconsolidated soft rocks accommodate stress in a penetrative plastic manner; in the model, this mechanical behaviour is represented by an unbonded DE material. Diagenesis is characterised by compaction and cementation; in the model, discs are shrunk according to their current burial depth; cementation is simulated by bond installation between discs whose displacements relative to each other are sufficiently small. (2) Complete elastic accommodation of stresses occurs in low-stress regions; in the model, they are characterised by an intact grid of bonds (MAT18-B). (3) Incidental fault activity at small-scale tectonic elements indicates distributed plastic deformation behaviour; its model representation is characterised by scattered discrete displacements due to the failure of individual bonds along favourably oriented planes of weakness; breakage and healing of bonds often alternate. (4) Localised plastic deformation along major faults is a product of strain canalisation due to persistent or repeated activity of individual planes; in the model,

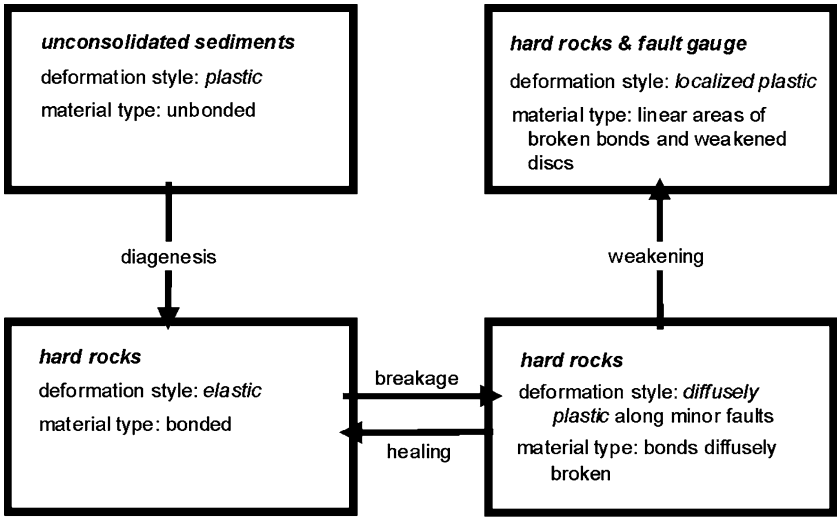

Fig. 5 Types of rock behaviour considered by the models material description. See text for additional information

significantly weakened discs make up those linear fault-zones (MAT18-W).

Results of a pure-shear extension experiment, performed in order to test the sensitivity of the critical strain-rate criteria $\dot{\varepsilon}_{cw}$ and $\dot{\varepsilon}_{ch}$, have proved that the processes addressed by the models are reproduced in a geologically plausible way (Seyferth, submitted). While the dip angle of individual fault segments detected by the AFC technique varies over a larger range, fault dip angles observed on a large scale are in good agreement with analytical solutions, predicting some 30° to σ_1 (Anderson 1951). Fault patterns in the models evolve self-organising. Conservation of volume and mass in the models is guaranteed by a disc property update algorithm, which enlarges strongly interpenetrating weakened discs (MAT18-W) and decreases their densities in return. While no buoyancy effects due to artificial density scaling have been observed, conservation of volume is affected by a small error ($<0.1\%$) due to the actual configuration of weakened/non-weakened discs.

Numerical experiments on halfgrabens

Model set-up and boundary conditions

In order to test the applicability of refined DE modelling techniques for the simulation of basin-scale tectonics and sedimentation, a common type of structural style has been selected and the numerical results compared with analogue models traditionally used in this kind of basin studies. The basic scenario is extension along major detachments leading to sedimentary basin formation by hanging wall collapse (Fig. 6a, b). This is found in a number of geodynamic settings, including continental extensional regimes and deltaic systems (e.g. Coward et al. 1987; Price and Cosgrove 1990; Busby and Ingersoll 1995).

The geometries of the resulting halfgrabens and fault systems in the pre- and syntectonic successions, respectively, depend largely on the geometry of the main basin-bounding fault and the mechanical properties of the hanging wall rocks. We present three model setups with different detachment shapes; two with a simple listric detachment and one with a more complex ramp–flat–ramp geometry. All detachments are composed of circular arc sectors. Extension of the initially 40 km wide models is driven by moving the wall segments along the detachment, whereas the right wall is displaced horizontally (Fig. 6c). The geometries and boundary conditions of these high-resolution DEM models are inspired by Ellis and McClay's (1988) analogue models. There, a thin plastic sheet was attached to the moving wall and pulled along the detachment, which imposes, in general, a fault parallel slip field onto the hanging wall (Fig. 6d). The height and depth-to-detachment of the models, respectively, imply a corresponding thickness of 15 km of the crustal brittle layer. Such a rheological structure is commonly inferred from the depth distributions of earthquakes in continental rift settings with moderate surface heat flows (Ruppel 1995), while at greater depths ductile deformation prevails.

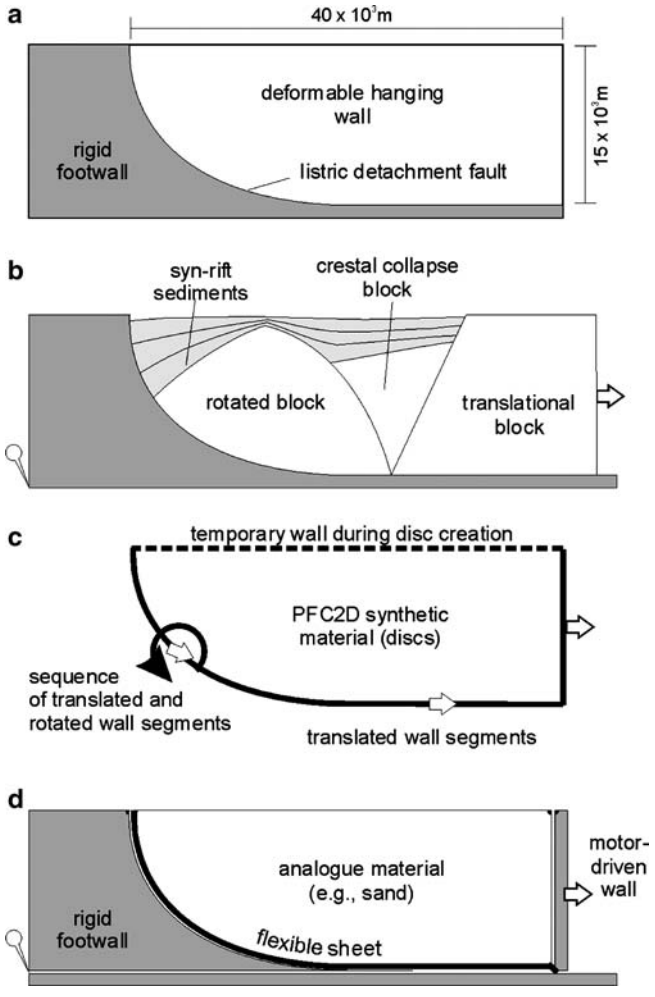

Fig. 6 Modelling concepts. (**a**) Initial setup of the conceptual model and (**b**) situation after model extension. (**c**) Corresponding setup of the DE models used in this study. (**d**) Setup of respective sandbox models (simplified after Ellis and McClay 1988); the basal velocity of the hanging wall block is kept constant by implementing a flexible sheet that is pulled to the right by the moving wall

DE modelling starts with confining the model domain using walls and randomly creating up to 20,000 small discs; subsequently, the disc radii are increased by a constant factor to achieve final porosity and a first state of mechanical equilibrium is computed, so that packing properties are equivalent to those used at the numerical test experiments discussed above. After applying gravity as a body force and computing a second equilibrium, contact-bonds are installed at any locus of disc contact (Fig. 2b). During the model run, the models are extended by 25% of their initial length, i.e. by a total amount of 10 km. Although the calculations are performed in a quasistatic manner and are, therefore, largely independent of real time; 'geologic'

time can be calculated from the rate of extension, which in turn controls the strain accumulated during a certain number of time steps. Models assume a constant crustal stretching velocity of 1 cm/a, an intermediate value within the range of possible extension rates for individual basins and lithospheric plate velocities.

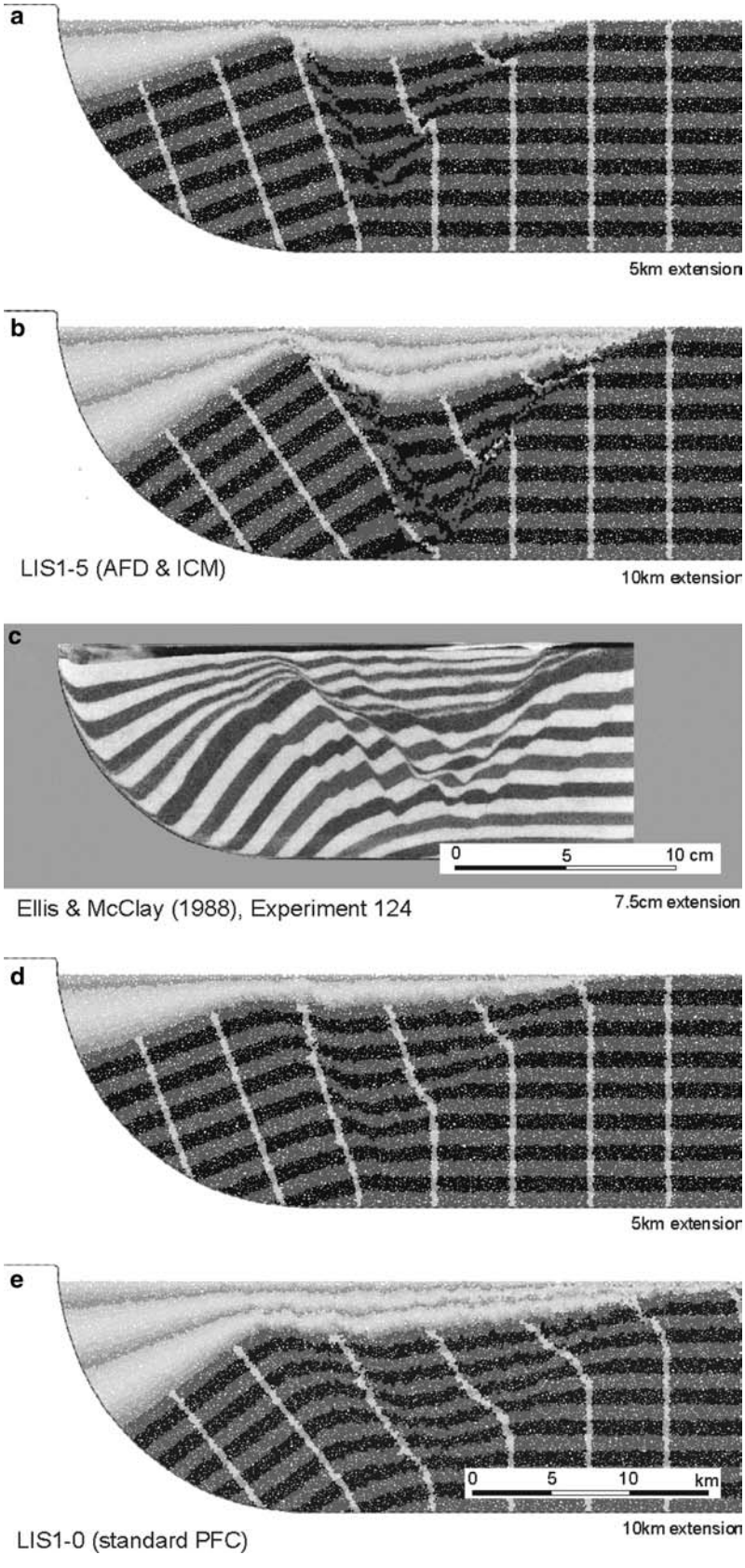

Fig. 7 Disc pattern in the models LIS1-5 (**a**, **b**) and LIS1-0 (**d**, **e**) after a5 and 10 km extension, respectively. (**c**) Sandbox experiment 124 by Ellis and McClay (1988), after 50% (15 cm) extension, which is equivalent to 11.25 km extension in the DE models

Based on the elapsed time, cycling is periodically halted to account for crack healing (ICM) and the disc property update (e.g. controlling sediment compaction) after each $\Delta t_h = \Delta t_d = 2{,}500$ a (Fig. 2c). Controlled by a larger time increment $\Delta t_w = \Delta t_s = 50{,}000$ a, disc weakening (AFD) and sedimentation is computed.

These numerical modelling results are finally compared to the corresponding analogue models of Ellis and McClay (1988). However, a 1:1 reproduction is not intended as the DEM models are based on material properties that are slightly different, i.e. Byerlee's empirical constants, and use features, like variable mechanical properties, to account for diagenesis and fault zone weakening that are not included in the analogue models.

Experiment I: detachment with 90° listric fault geometry (LIS1)

In the first experiment, sedimentary basin formation in relation to extension along a listric detachment, with an initial dip of 90° close to the breakaway, was studied. The resulting disc configurations, after 5 and 10 km extensions, are shown in Fig. 7a, b. For comparison, a corresponding sandbox experiment of Ellis and McClay (1988; their experiment 124), albeit for larger amounts of extension, is also shown (Fig. 7c).

The high-resolution DEM models are capable of reproducing in detail tectonic features, which typically form in this kind of extensional scenario. Close to the fault, a largely undeformed hanging wall block was rotated counter-clockwise, forming a large rollover anticline and halfgraben structure above. Further away from the breakaway, a second, more symmetrical subbasin had formed. This so-called crestal collapse graben was bounded by an upward convex antithetic fault and a planar synthetic fault. The antithetic fault initially nucleated at the point where the detachment soles out and progressively migrates parallel to the flat part of the fault, during further extension; thus forming the non-rotated margin and outer limit of basin formation. The other normal fault bounding the crestal collapse graben is progressively rotated together with the leftmost block leading to the formation of secondary synthetic normal faults. In the deeper part of the model, where syn- and antithetic faults meet beneath the crestal collapse graben, a complex fault pattern results. Faulting does not only affect the pretectonic and basement rocks, respectively, but faults also continue upward into the syntectonic sediments. There, vertical displacements decrease with younger deposition ages.

In summary, the experiment with the 90° listric detachment geometry produced a sedimentary basin with two main depocentres separated by an intervening high, with strongly reduced thicknesses of syntectonic sediments. This basin architecture results from two basic deformation styles in the hanging wall, i.e. fault block rotation close to the detachment breakaway and translation above the flat part of the master fault. Numerical modelling results are in broad agreement with comparable sandbox experiments (Ellis and McClay 1988; their experiment 124), which show a very similar structural style and sequence of faulting (Fig. 7c). In this experiment, the initially 15 cm long hanging wall, made up of homogeneous sand, was stretched by 50%, which is equivalent to a 7.5 cm displacement of the moving wall and an 11.25 km extension in our DE models, respectively. Since both the numerical and the analogue models are designed to apply a constant shear velocity to the base of the hanging wall, the bending of sand strata visible in the sandbox pictures seems to be a surprising difference to the DEM results. However, it is caused by a boundary effect at the front glass wall of the deformation rig (Ellis and McClay 1988), which is not present in the numerical counterpart.

The development of a fault pattern comparable to the analogue sandbox experiments is a consequence of the enhancements of the DE modelling techniques, namely the AFD and ICM techniques described above. Without these improvements, no strain localisation and differential displacements along discrete planes would occur. The difference is shown in Fig. 7d, e. There, a standard bonded PFC2D model material is used, which results only in a diffuse, 'smeared' deformation of the hanging wall rocks and no fault detection, either in the pre- or the post-tectonic strata, is possible. This difference is also illustrated by Fig. 8, which shows a comparison of the contact-bond pattern between models with and without AFD and IFC implementation. Model LIS1-5 is affected by disc weakening

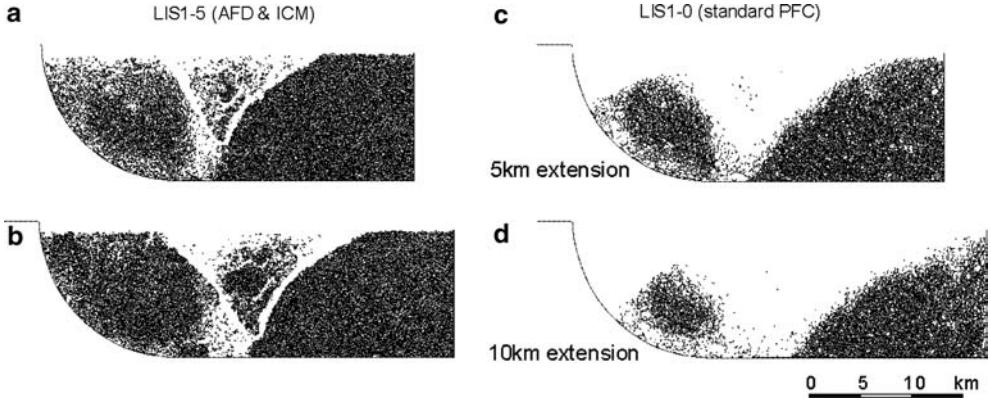

Fig. 8 Contact-bond pattern in models LIS1-5 and LIS1-0 after 5 km (**a**, **c**) and 10 km extension (**b**, **d**), respectively. Model LIS1-5 (**a**, **b**) is affected by disc weakening

(minimum strain rate $\dot{\varepsilon}_{cw} = 1 \times 10^{-13}\,s^{-1}$) and crack healing (maximum strain rate $\dot{\varepsilon}_{ch} = 1 \times 10^{-15}\,s^{-1}$), which results in the localisation of broken bonds along narrow zones (Fig. 8a, b). In addition, syn-rift sediments in the evolving basins have been bonded to a large extent. In contrast, model LIS1-0, which uses standard PFC without any localisation techniques, shows large areas where bonds have broken areally (Fig. 8c, d).

Experiment II: detachment with 60° listric fault geometry (LIS2)

This experiment differs from the previous one in a shallower dip of the detachment near the breakaway, i.e. 60° instead of 90°. Because of the decreased fault curvature, a larger portion of the hanging wall block was affected by rotational movements, although the absolute angle of rotation was smaller. As a consequence, a large rollover anticline develops and two smaller crestal collapse grabens successively form in the hanging wall block (Fig. 9a–c). Figure 9b shows the current state of rock behaviour after a 10 km extension.

During the initial stages of extension, a collapse graben first forms furthest away from the breakaway, in relation to the major planar antithetic normal fault, which cuts through the entire hanging wall. The other side of the graben is defined by an almost vertical normal fault. As extension progresses, a new crestal collapse graben forms closer to the breakaway due to continued rotation of the hanging wall. Again, the antithetic fault

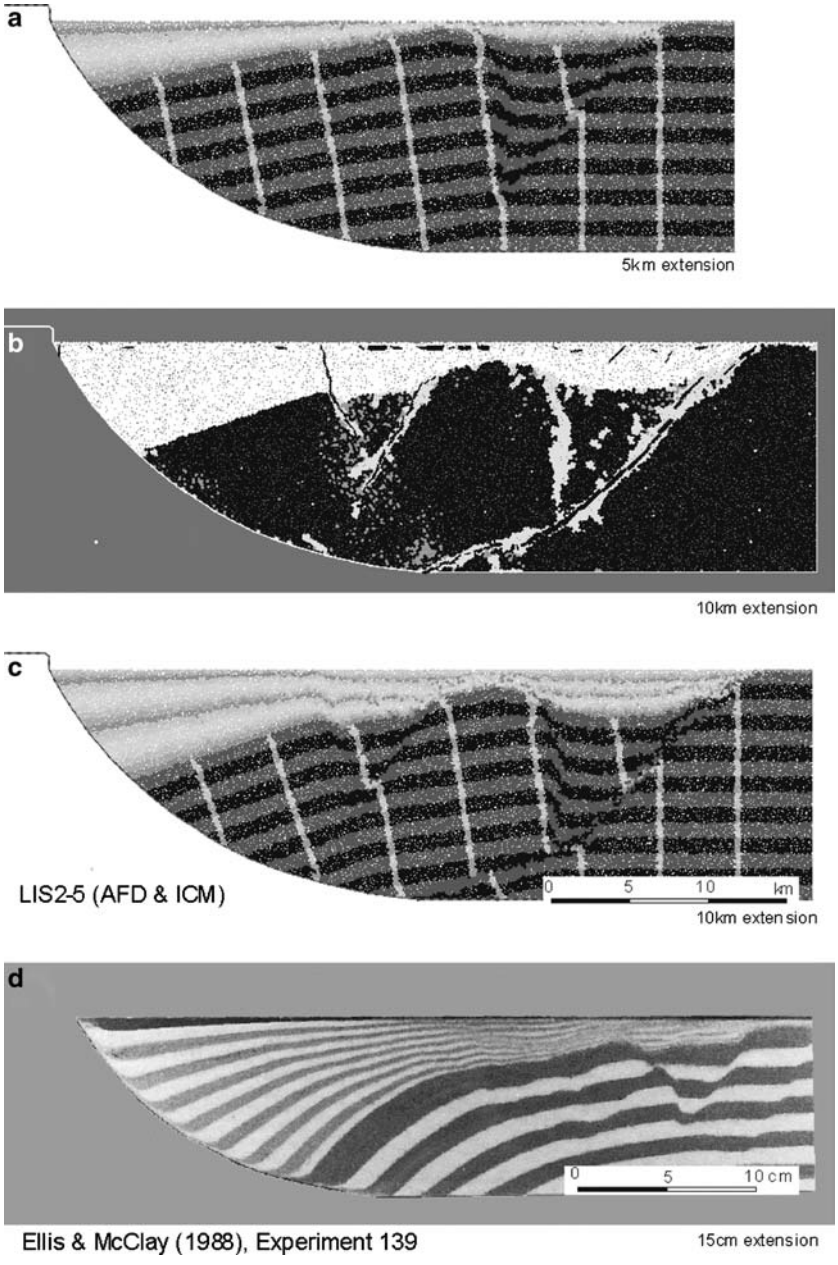

Fig. 9 Disc pattern in the model LIS2-5 after (**a**) 5 km and (**c**) 10 km extension. (**b**) Inferred type of mechanical rock behaviour after 10 km extension: *black* mainly elastic, *dark grey* plastic with minor faults, *light grey* weakened by major faults, *white* unconsolidated sediments and sediments in diagenesis; *black lines* illustrate the currently active fault pattern (thin lines < 0.5 mm/year, medium 0.5–1 mm/year, thick > 1 mm/year). (**d**) Sandbox experiment 139 by Ellis and McClay (1988) after 50% (7.5 cm) extension, which is equivalent to 11.5 km extension in the DE models

dominates over the synthetic one and some of the basement faults continue upwardly into the syntectonic sediments. The numerical simulation results compare favourably with a corresponding analogue model of Ellis and McClay (1988; their experiment 139), which also shows a broad halfgraben geometry and the successive development of small crestal collapse grabens (Fig. 9d). In this experiment, the initially 30 cm long hanging wall, made up of sand and mica layers, was stretched by 50%, which is equivalent to a 15 cm displacement of the moving wall and a 22.5 km extension in our DE models, respectively. As in the DEM model, graben formation also migrates toward the detachment breakaway as extension proceeds.

Experiment III: detachment with ramp–flat–ramp fault geometry

The third scenario uses a more complex detachment geometry, i.e. two steeply dipping (90°) listric sections separated by a flat fault segment at 7 km depth. The disc configurations after a 5 and 10 km extension, calculated for model RFR2-5, are shown in Figs. 10a–c and 11a–c;

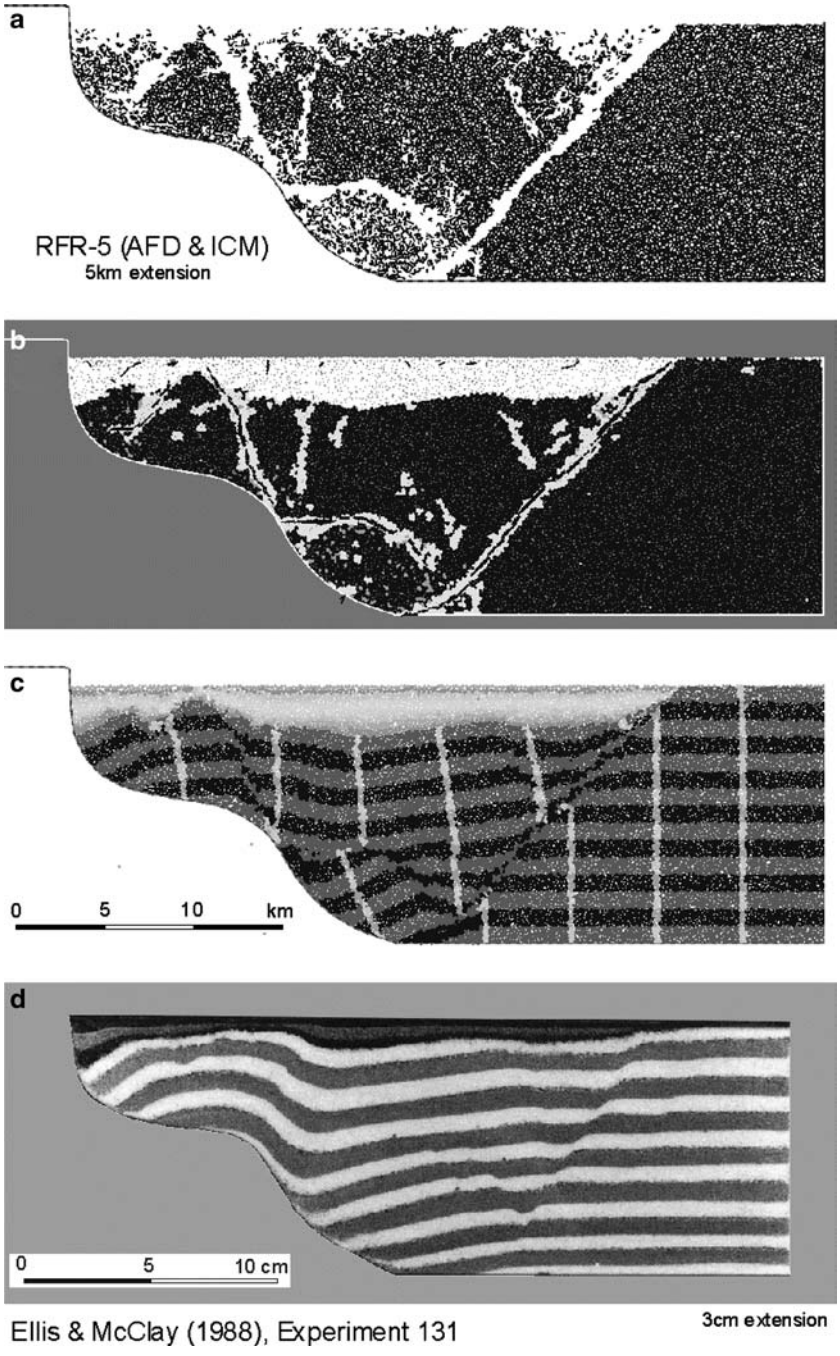

Fig. 10 Model RFR-5 after 5 km extension. **a** Pattern of active contact-bonds. **b** Inferred type of mechanical rock behaviour; for explanation see Fig. 9b. **c** Disc pattern showing pre- and syn-rift strata. **d** Sandbox experiment 131 by Ellis and McClay (1988), after 12% (3 cm) extension, which is equivalent to 4.5 km extension in the DE models

whereas corresponding analogue models are presented in Figs. 10d and 11d, respectively.

Block rotation in relation to the two ramp segments results in the formation of two pairs of rollover anticlines and crestal collapse grabens that partly overlap. Basement deformation, near the detachment breakaway, proceeds in a manner similar to experiment I (Fig. 7), albeit at a smaller scale. Near the lower ramp, a second rotated fault block forms, which is completely bounded by faults, some of which are low-angle normal faults (Fig. 10a–c). This block has been rotated by about 45° after 10 km, whereas the basement block near the upper ramp is turned in an almost upright position (Fig. 11c). As in the previous experiments, a major antithetic normal fault nucleates at the point where the detachment flattens out. It forms the outer limit of basement deformation and is translated, without rotation, during subsequent extensions. The lower ramp projects through the overlying strata and forms a synthetic normal fault.

During further extension the upper hanging wall block is carried over the flat fault segment and down the second ramp. This results in a reversal of the rotation direction of the corresponding fault block, i.e. first counter-clockwise and then clockwise, as it is tilted over the lower ramp. As a result, reverse faults, nucleating at the kink between the flat and the ramp part of the detachment, are formed, which partly overprints the structures formed earlier. These reverse faults continue into the basin sediments (Fig. 11c) and illustrate how synsedimentary tectonics with reverse faulting, can occur in an overall extensional regime.

The modelling results can be compared to the analogue experiment 131 of Ellis and McClay (1988), whose hanging wall had an initial length of 25 cm and was

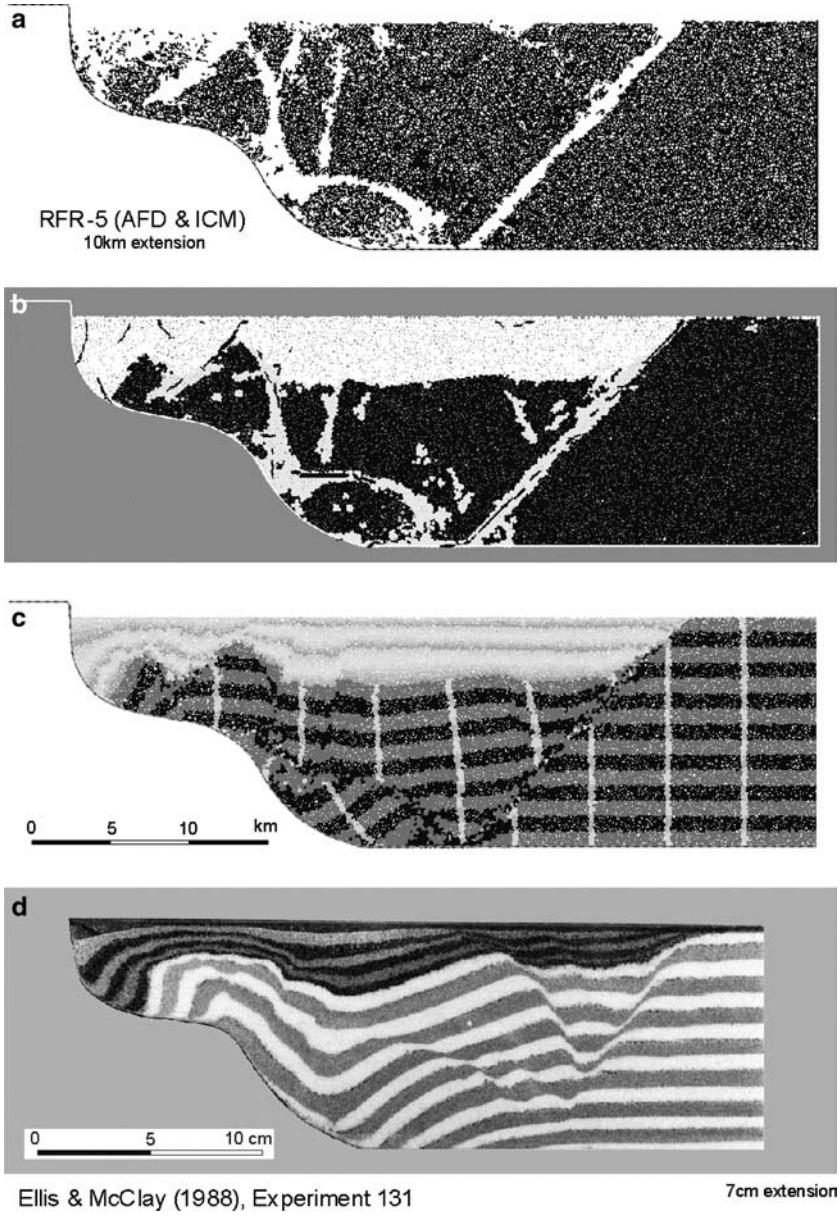

Fig. 11 Model RFR-5 after 10 km extension. **a** Pattern of active contact-bonds. **b** Inferred type of mechanical rock behaviour; for explanation see Fig. 9b. **c** Disc pattern showing pre- and syn-rift strata. **d** Sandbox experiment 131 by Ellis and McClay (1988), after 28% (7 cm) extension, which is equivalent to 10.5 km extension in the DE models

made up of sand and mica layers. Figures 10d and 11d show this experiment after 12% (3 cm) extension and 28% (7 cm) extension, which is equivalent to a 4.5 and 10.5 km extension in the DE models, respectively. The numerical simulation reproduces the overall basin architecture and fault style, consisting of two rollover anticlines with crestal collapse grabens, separated by a hanging wall syncline. As before, reverse faults form and overprint the initially formed structures as the upper hanging wall block is dragged over the detachment crest. The lower rotated fault block is bounded by a concave upward normal fault.

Discussion and conclusions

The three numerical experiments presented above demonstrate that DE models can be used to study basin-scale fault systems and syntectonic sedimentation in considerable detail, provided their resolution is large enough and enhanced modelling techniques are used, i.e. AFC and ICM algorithms. As a consequence, discrete fault planes can develop in the synthetic material; the evolving structural pattern and the resulting distribution of strata modelling results are comparable to respective analogue models. In addition, the DE models provide valuable insights into the internal state of the synthetic material (e.g. the distribution of failed contact-bonds and the occurrence of weakened discs). Based on that, different types of rock behaviour can be inferred and interpreted geologically. However, it should be kept in mind that there is no direct correlation between the geometry and pattern of individual discs or bonds and the structure of the modelled natural rock masses, since the length scale of dislocation planes vary over several orders of magnitudes within the latter. Rather, the model information may be used as a proxy for the predominant mechanical behaviour of rocks in the respective part of the model.

At present, one of the main advantages of analogue modelling approaches remains the attainable resolution. The presented DE models have been processed using a small workstation cluster (3×1.0 GHz), where a complete model run took about 10 days. As a consequence, reasonable computing times limit the model resolution to a disc size about five times coarser than the grain size in classical sandbox models. However, since disc weakening by the AFD algorithm provides efficient narrow dislocation planes, the resolution ratio diminishes to a value of three, if the width of an individual granular shear zone is addressed. Anticipating further improvements in low-cost computing power and/or intense use of parallel processing, a 2D resolution of DE models directly comparable to the sandbox models will soon be available.

Using the techniques outlined above, the DEM can then offer a number of benefits over the classical sandbox approach, with respect to the setup of the models, the mechanical material properties characterising crustal rocks as well as the evaluation and post-processing of the results. Although sandbox models inspired the model setup used in this study, the modelling approach is, of course, generally applicable and not restricted by the limits of mechanically induced boundary conditions. Thus, more complex scenarios can be simulated, e.g. differential uplift of the model base due to isostatic response within the footwall block, or a more realistic distribution of syn-rift sediments; the respective processes may be described by the output of external numerical modelling. Similarly, modelling is not restricted by the available analogue materials, since using the calibration procedures outlined above, almost any rock mechanical data can be transferred into appropriate microproperties of a DE material. In addition, the presented approach is capable of simulate temporal changes in material behaviour, for example, compaction and diagenetic changes in rock strength, which is already accounted for in the present models.

A very promising improvement of the DE technique is the combination of structural calculations with fluid mechanics. Such a hydro-mechanical coupling in particle models has already been successfully performed on a small, core-size scale, in order to study stress-dependent permeabilities of reservoir rocks (Li and Holt 2002). Combining basin-scale fluid flow with the DE modelling techniques described above would bring a new dimension to basin modelling, as it would allow one to quantitatively consider, for example, undercompaction and overpressuring during basin evolution. This example shows that DEM still offers a large range of possibilities, both in developing refined modelling techniques as well as with respect to applications to real world settings.

Acknowledgements D.R. Burbidge and C. Pascal are thanked for their helpful comments on an earlier version of the manuscript. The study was funded by the Deutsche Forschungsgemeinschaft, whose support is gratefully acknowledged. N. Kukowski is thanked for their editorial help.

References

Anderson E (1951) The dynamics of faulting. Oliver and Boyd, London, pp 1–206

Baldwin B, Butler CO (1985) Compaction curves. AAPG Bull 69:622–626

Burbidge DR, Braun J (2002) Numerical models of the evolution of accretionary wedges and fold-and-thrust belts using the distinct-element method. Geophys J Int 148:542–561

Busby CJ, Ingersoll RV (1995) Tectonics of sedimentary basins. Blackwell Science, Oxford, pp 1–579

Byerlee JD (1978) Friction of rocks. Pure Appl Geophys 116:615–626

Coward MP, Dewey JF, Hancock PL (1987) Continental extensional tectonics. Geol Soc Spec Publ 28:1–637

Cundall PA (1971) A computer model for simulating progressive large scale movements in blocky rock systems. In: Proceedings of the Symposium of the International Society for Rock Mechanics, vol 1. Nancy, France, Paper No. II-8

Cundall PA, Strack ODL (1979) A discrete numerical model for granular assemblies. Géotechnique 29:47–65

Dalguer LA, Ikikura K, Riera JD (2003) Generation of new cracks accompanied by the dynamic shear rupture propagation of the 2000 Tottori (Japan) earthquake. Bull Seismol Soc Am 93:2236–2252

Diederichs MS, Kaiser PK, Eberhardt E (2004) Damage initiation and propagation in hard rock during tunnelling and the influence of near-face stress rotation. Int J Rock Mech Mining Sci 41:785–812

Ellis PG, McClay KR (1988) Listric extensional fault systems; results of analogue model experiments. Basin Res 1:55–70

Erickson SG, Strayer LM, Suppe J (2001) Initiation and reactivation of faults during movement over a thrust-fault ramp: numerical mechanical models. J Struct Geol 23:11–23

Holt RM, Doornhof D, Kenter CJ (2003) Use of discrete particle modeling to understand stress-release effects on mechanical and petrophysical behavior of granular rocks. In: Konietzky H (ed) Numerical modeling in micromechanics via particle methods. Swets& Zeitlinger, Lisse, pp 269–276

Hubbert MK, Rubey WW (1959) Role of fluid pressure in the mechanics of overthrust faulting. Bull Geol Soc Am 70:115–205

Itasca (1999) PFC2D—Particle Flow Code in 2 Dimensions. Theory and background. Itasca Consulting Group, Minneapolis, MN, pp 1–124

Li L, Holt RM (2002) Particle scale reservoir mechanics. Oil Gas Sci Technol 57:525–538

McClay KR (1989) Physical models of structural styles during extension. In: Tankard AJ, Balkwill HR (eds) Extensional tectonics and stratigraphy of the North Atlantic margins. AAPG Memoir, vol 46, pp 95–110

Mora P, Place D (1993) A lattice solid model for the nonlinear dynamics of earthquakes. Int J Mod Phys C4:1059–1074

Mora P, Place D (1998) Numerical simulation of earthquake faults with gouge: toward a comprehensive explanation for the heat flow paradox. J Geophy Res 103:21067–21089

Morgan JK, Boettcher MS (1999) Numerical simulations of granular shear zones using the distinct element method—1. Shear zone kinematics and the micromechanics of localization. J Geophys Res 104:2703–2719

Peshkin MA, Sanderson AC (1989) Minimization of energy in quasi-static manipulation. IEEE Trans Robotics Autom 5:53–60

Price NJ, Cosgrove NJ (1990) Analysis of geological structures. Cambridge University Press, Cambridge, pp 187–208

Ruppel C (1995) Extensional processes in continental lithosphere. J Geophys Res 100:24187–24215

Rutter EH, Holdsworth RE, Knipe RJ (2001) The nature and tectonic significance of fault-zone weakening: an introduction. In: Holdsworth RE, Strachan RA, Macloughlin JF, Knipe RJ (eds) The nature and tectonic significance of fault-zone weakening. Geol Soc Spec Publ 186:1–11

Sainsbury DP, Cai Y, Hebblewhite BK (2003) Numerical investigation of crown pillar recovery beneath stabilized rockfill. In: Konietzky H (ed) Numerical modeling in micromechanics via particle methods. Swets& Zeitlinger, Lisse, pp 225–231

Saltzer SD, Pollard DD (1992) Distinct element modeling of structures formed in sedimentary overburden by extensional reactivation of basement normal faults. Tectonics 11:165–174

Scott DR (1996) Seismicity and stress rotation in a granular model of the brittle crust. Nature 381:592–595

Seyferth M, Henk A (2002) Coupled DEM and FEM models: an approach to bridge the gap between large-scale geodynamic and high-resolution tectonic modeling. EOS Transactions (Fall Meeting Suppl) 83:1376–1377

Strayer LM, Suppe J (2002) Out-of-plane motion of a thrust sheet during along-strike propagation of a thrust ramp: a distinct-element approach. J Struct Geol 24:637–650

Vietor T (2003) Numerical simulation of collisional orogeny using the distinct element technique. In: Konietzky H (ed) Numerical modeling in micromechanics via particle methods. Swets& Zeitlinger, Lisse, pp 295–301

Wang C, Tannant DD, Lilly PA (2003) Numerical analysis of the stability of heavily jointed rock slopes using PFC2D. Int J Rock Mech Mining Sci 40:415–424